
Article:
Serna-Gallén, P., Beltrán-Mir, H., Cordoncillo, E. et al. (3 more authors) (2019) Site-selective symmetries of Eu3+-doped BaTiO3 ceramics: a structural elucidation by optical spectroscopy. Journal of Materials Chemistry C, 7 (44). pp. 13976-13985. ISSN 2050-7526

https://doi.org/10.1039/c9tc03987b

Site-selective symmetries of Eu^{3+}-doped $BaTiO_3$ ceramics: a structural elucidation by optical spectroscopy

P. Serna-Gallén[1], H. Beltrán-Mir[1], E. Cordoncillo[1], A. R. West[2], R. Balda[3], J. Fernández[3]

[1]*Departamento de Química Inorgánica y Orgánica, Universidad Jaume I, Av. Sos Baynat s/n 12071, Castelló de la Plana, Spain*

[2]*Department of Materials Science & Engineering, University of Sheffield, Mappin Street, Sheffield S1 3JD, U.K*

[3]*Departamento de Física Aplicada I, Escuela de Ingeniería de Bilbao, Universidad del País Vasco UPV-EHU, 48013 Bilbao, Spain.*

Materials Physics Center CSIC-UPV/EHU, 20018 San Sebastian, Spain.

Donostia International Physics Center DIPC, 20018 San Sebastian, Spain

---

Abstract

Eu^{3+}-doped $BaTiO_3$ ceramics with a dopant content between 0–10 mol% were prepared by sol-gel synthesis based on the nominal compositions $(Ba_{1-3x}Eu_{2x})TiO_3$ and $Ba(Ti_{1-x}Eu_x)O_{3-x/2}$, where two possible substitution mechanisms are addressed. By means of optical spectroscopy, our study gives a plausible elucidation of Eu^{3+} site occupation in micrometric $BaTiO_3$ particles. Time-resolved fluorescence line narrowing shows the presence of five different crystal field sites for europium ions and possible symmetries are inferred for each one. The solubility limit of the lanthanide ion was found to be about 3 mol%. The experimental results are consistent with the preference of Eu^{3+} to occupy Ba^{2+} sites regardless of the nominal compositions and substitution mechanism. However, low concentrations of the dopant also occupied Ti^{4+} sites, highlighting the amphoteric character of Eu^{3+}. In addition, the existence of anti-Stokes and Stokes vibronic sidebands in the $^5D_0 \rightarrow {}^7F_{0,1}$ transitions of Eu^{3+} ions is confirmed. This important issue can explain the lack of resolution found in the room temperature spectra of these transitions due to vibronic mixing of the excited levels. Thereby, the existence of non-equivalent europium sites with different spectroscopic properties could have a great impact not only on the optical properties of doped-$BaTiO_3$ ceramics but also on their wide range of electronic properties and device applications.

Keywords: barium titanate, europium, optical spectroscopy, luminescence, crystal field, substitution site

1. Introduction

Technological developments are guided by a progressive dynamic which meets the industrial needs requested by a more and more challenging market environment. Barium titanate, $BaTiO_3$, has been a longstanding material for electronic devices due to its broad spectrum of properties, such as spontaneous polarization, high dielectric permittivity in the paraelectric phase and piezoelectric response [1]. It is well known the nature of impurities plays a significant role to modify the characteristics of pristine materials. Luminescent trivalent lanthanide ions (Ln^{3+}) incorporated into solids have been greatly studied not only because of their application in emission displays or lasers but also for their ability to change and tune the properties of the material depending on the site occupation of Ln^{3+} in the host lattice [2]. Indeed, Ln^{3+}-doped $BaTiO_3$ has shown outstanding performance to be used in ferroelectric capacitors due to its colossal dielectric constant[3].

In this way, some studies have been focused on doping $BaTiO_3$ ceramics with Ln^{3+} and trying to establish the position of the ion. Elucidating the distribution of Ln^{3+} involves determining if it occupies a single site (Ba^{2+} or Ti^{4+}) or multiple sites (both Ba^{2+} and Ti^{4+}), the solubility limit in each site, and how this distribution changes with lanthanide concentration [4–7]. According to different authors, the structural preference is Ba^{2+} site for larger ions (La–Sm), while for smaller ions (Yb, Lu) the substitution takes place in Ti^{4+} site. For intermediate ions (Gd, Dy, Ho, Er), it is highlighted their amphoteric behaviour, being able to occupy both Ba^{2+} and Ti^{4+} positions.

However, there is still some controversy for Eu dopant. Eu lies between Sm and Gd in the lanthanide series and therefore could show slight amphoteric character like Gd. Ba^{2+} has an ionic radius of 1.610 Å (for a 12 coordination number, CN), while Ti^{4+} has an ionic radius of 0.605 Å (for a CN=6). Eu^{3+} has an intermediate radius of 0.947Å (for a CN=12) and 1.226Å (for a CN=6) [8]. These similar values make it possible for Eu^{3+} to occupy both sites.

What is more, Eu distribution has been reported to be influenced by the nominal formula and synthesis procedure of $BaTiO_3$ compounds. In fact, different properties and

distributions of the ion are described depending on the size of the particles (nanocrystals or micrometric materials) and the substitution mechanism postulated. According to X-ray diffraction (XRD) data, luminescence analysis or electrical measurements, some studies have confirmed the presence of Eu in Ba^{2+} site [4,9], while others have concluded that Eu occupies both Ba^{2+} and Ti^{4+} sites [4,8,10]. It has also been postulated that the mechanism of substitution could depend on Eu concentration. Figure 1 depicts a ternary phase diagram, which highlights the different ionic compensation mechanisms that can be drawn as follows:

(1) $(Ba_{1-3x}Eu_{2x})TiO_3$, with the creation of barium vacancies and Eu^{3+} occupying Ba^{2+} site.

(2) $(Ba_{1-x}Eu_x)Ti_{1-x/4}O_3$, with the creation of titanium vacancies and Eu^{3+} occupying Ba^{2+} site.

(3) $(Ba_{1-x}Ti_{1-x}Eu_{2x})O_3$, with a double substitution of Eu^{3+}.

(4) $Ba(Ti_{1-x}Eu_x)O_{3-x/2}$, with the creation of oxygen vacancies and Eu^{3+} occupying Ti^{4+} site.

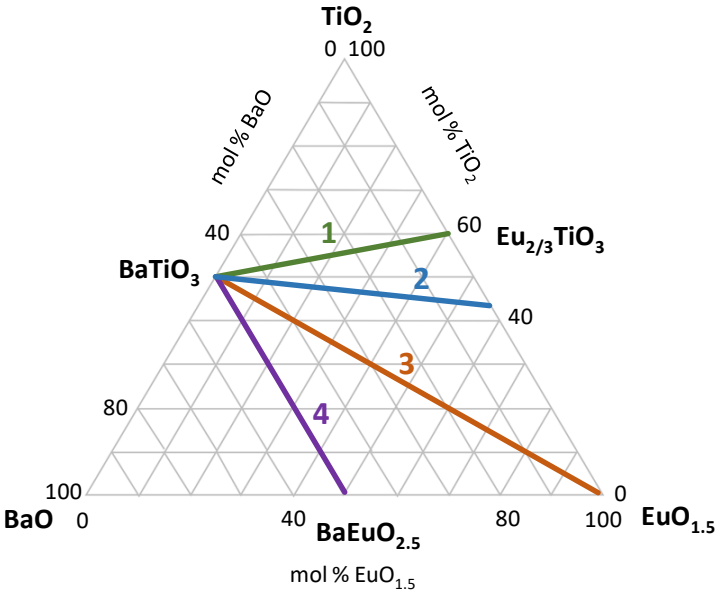

Figure 1. Ternary phase diagram for the different ionic compensation mechanisms.

In any case, the presence of structural defects modifies the local crystal-field symmetry and strength and may lead to a variety of non-equivalent europium centres, which could affect the optical properties of $BaTiO_3$ ceramics [11]. Unfortunately, to the best of our knowledge, no accurate studies about this have been performed.

Thereby, the purpose of the present work is to study Eu^{3+}-doped $BaTiO_3$ ceramics synthesised via sol-gel method describing the crystallographic nature of non-equivalent

europium sites and giving plausible reasoning of them. For this, compounds have been synthesised according to two possible mechanisms of substitution. The first one, addressed as *Ba-mechanism*, has the nominal formula $(Ba_{1-3x}Eu_{2x})TiO_3$. This mechanism (1 in Figure 1) has been reported for nanocrystals but not for micrometric materials and implies that Eu occupies only Ba^{2+} site. The second mechanism (4 in Figure 1), referred to as *Ti-mechanism*, has the nominal formula $Ba(Ti_{1-x}Eu_x)O_{3-x/2}$ and raises that Eu is only present in Ti^{4+} site.

Herein, it has been carried out the study of the site-resolved luminescence of Eu^{3+} in $BaTiO_3$ ceramics, bearing in mind the adequacy of the dopant ion as a structural probe. Since the $^5D_0$ state is nondegenerate under any symmetry, the structure of the $^5D_0 \rightarrow {}^7F_J$ emission is only determined by the splitting of the terminal levels caused by the local crystal field. Moreover, as the $^7F_0$ level is also nondegenerate, site-selective excitation within the inhomogeneous broadened $^7F_0 \rightarrow {}^5D_0$ absorption band can be performed by using the fluorescence line-narrowing (FLN) technique to distinguish among different local environments around the lanthanide ions [11–13].

2. Experimental section

2.1. Materials

Barium acetate [$Ba(OAc)_2$ 99%], titanium(IV) isopropoxide [$Ti(OPr^i)_4$ 98%] and europium(III) acetate [$Eu(OAc)_3$ 99.9%] were purchased from Strem Chemicals. Acetylacetone [acacH 99.8%] was supplied by Panreac. Glacial acetic acid [HOAc 99.5%] was a product of Labkerm and methanol [MeOH 99.8%] was obtained from Scharlau.

2.2. Synthesis of Eu^{3+}-doped $BaTiO_3$ compounds

Samples with 0, 1, 2, 3, 4, 5 and 10 mol% Eu^{3+} content for each proposed mechanism (*Ba* or *Ti-mechanism*) were synthesised via sol-gel method according to the process reported in previous studies [14]. The molar ratios of reagents and solvents were $1Ba^{2+}$: $21H_2O$: 40MeOH and $1Ti^{4+}$: 8acacH. The dried gel was ground and the fine powder was fired at 1200ºC in air for two hours, obtaining micrometric materials. To carry out optical analysis, pellets of the fired powders were made and sintered at 1200ºC in air for two hours. For convenience, the following abbreviations are used throughout the remainder of the Article: "0%-BT" (for pure $BaTiO_3$), "*n*%-Ba" (for samples of *Ba-mechanism*) and

"*n*%-Ti" (for samples of *Ti-mechanism*), where *n* takes the values {1, 2, 3, 4, 5, 10} and indicates the molar percentage of Eu^{3+} in the sample.

2.3. Characterisation

Powder X-ray diffraction (XRD) measurements were performed using a Bruker D4-Endeavor X-ray diffractometer with CuK_α radiation at a scan speed of 0.3º/min. All data were collected between $15 \leq º\, 2\theta \leq 70$ at room temperature. With the aim of calibrating the peak positions of the XRD pattern, an internal standard of Si NIST (SRM 640e) was used. Lattice parameters were refined using $WinX^{POW}$ 1.06 software version.

The microstructure of samples was observed using a JEOL 7001F scanning electronic microscope (SEM) equipped with a spectrometer for energy dispersive analysis of X-rays (EDX). The operation parameters were: an acceleration voltage of 15 kV, a measuring time of 20 s and a working distance of 10 mm.

Different optical properties were studied for fired Eu^{3+}-doped $BaTiO_3$ samples. Emission measurements were performed at room temperature with an Eclipse Fluorescence Spectrophotometer (Varian). Spectra were recorded in the range between 550 and 750 nm upon excitation at 466 nm (corresponding to the hypersensitive $^7F_0 \rightarrow {}^5D_2$ transition). From the obtained spectra, the ratio *R* (defined as the ratio between the intensities of $^5D_0 \rightarrow {}^7F_2$ and $^5D_0 \rightarrow {}^7F_1$ transitions) and the Ω_2 Judd-Ofelt parameter were calculated.

Resonant time-resolved FLN spectra were performed by exciting the samples with a pulsed frequency doubled Nd:YAG pumped tunable dye laser of 9 ns pulse width and 0.08 cm^{-1} linewidth and detected by an EGG&PAR Optical Multichannel Analyzer. The measurements were carried out by keeping the sample temperature at 10 K in a closed cycle helium cryostat.

3. Results and discussion

3.1. Structural characterisation

XRD patterns of the fired samples show all the peaks corresponding to the tetragonal phase of barium titanate (JCPDS-ICDD card 5-626). No traces of crystalline secondary

phases such as $Eu_2Ti_2O_7$ are detected. It is only appreciated a secondary phase in 10%-Ti sample.

According to the ionic radius distribution, if Eu^{3+} occupies Ba^{2+} site, there will be a contraction in the unit cell volume (V_0) since Eu^{3+} is smaller than Ba^{2+}. In the opposite case, if Eu^{3+} occupies Ti^{4+} site, according to the same line of reasoning, we expect an expansion in V_0. Table 1 summarises the lattice parameters calculated. The evolution of V_0 and tetragonality (c/a) with Eu^{3+} concentration are also depicted in Figure 2 for samples of both mechanisms (*Ba* and *Ti-mechanisms*).

Table 1. Structural parameters of Eu^{3+}-doped $BaTiO_3$ samples.

Sample	a (Å)	c (Å)	V_0 (Å^3)	Sample	a (Å)	c (Å)	V_0 (Å^3)
0%-BT	3.9937(3)	4.0344(5)	64.347(7)	-	-	-	-
1%-Ba	3.9959(12)	4.0279(25)	64.313(21)	1%-Ti	3.9951(3)	4.0304(4)	64.329(6)
2%-Ba	3.9967(12)	4.0221(24)	64.247(17)	2%-Ti	3.9959(9)	4.0201(17)	64.19(3)
3%-Ba	3.9966(8)	4.0195(14)	64.202(10)	3%-Ti	3.9971(10)	4.0300(21)	64.386(23)
4%-Ba	3.9962(12)	4.0208(20)	64.212(15)	4%-Ti	3.9950(22)	4.035(5)	64.40(3)
5%-Ba	3.9967(5)	4.0192(13)	64.202(16)	5%-Ti	3.9960(16)	4.0329(12)	64.396(20)
10%-Ba	3.9964(14)	4.0204(24)	64.212(18)	10%-Ti	3.9971(11)	4.033(3)	64.43(3)

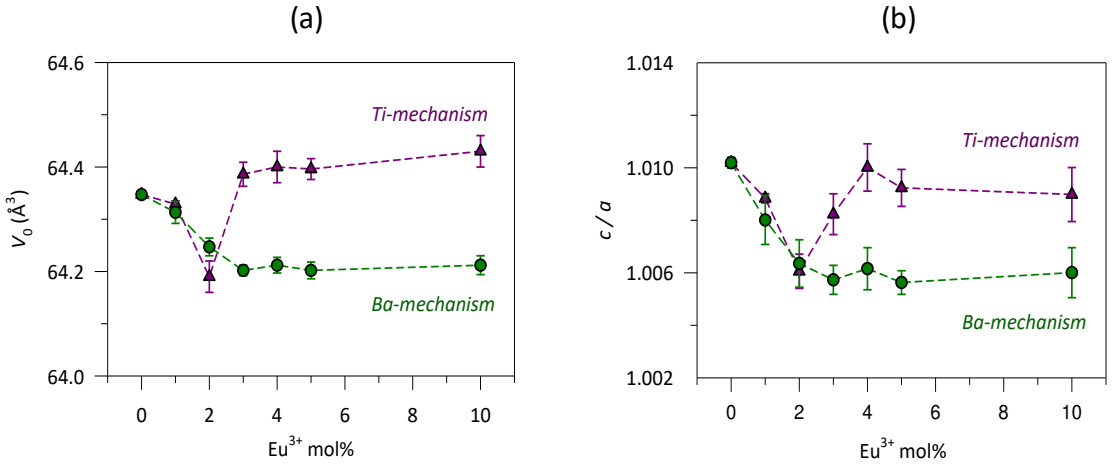

Figure 2. Evolution of V_0 (a) and c/a (b) with Eu^{3+} concentration for samples of *Ba* and *Ti-mechanisms*.

The evolution of V_0 and tetragonality with Eu^{3+} concentration has the same tendency, indicating a good correlation between these two parameters. Therefore, further

explanations will be addressed only for V_0. For samples of *Ba-mechanism*, there is a progressive decrease in V_0 up to 3 mol% of Eu^{3+}. This result suggests that a great majority of europium ions are incorporated into Ba^{2+} site. Despite this, lower concentrations of europium could also occupy Ti^{4+} site. For concentrations ≥ 3 mol%, V_0 remains almost constant, suggesting that no more dopant is entering in $BaTiO_3$ structure.

On the other hand, for samples of *Ti-mechanism*, we observed again a progressive decrease in V_0 up to 2 mol%, highlighting the preference of europium for occupying Ba^{2+} site. However, it is appreciated an important increase in V_0 at 3 mol%, which could be attributed to a higher concentration of europium ions occupying Ti^{4+} site. In other words, as in 3%-Ti sample there have been introduced Ti vacancies in the system according to the nominal formula of the mechanism, $Ba(Ti_{1-x}Eu_x)O_{3-x/2}$, once Ba^{2+} site is almost saturated, europium can occupy Ti^{4+} site in a greater proportion in contrast with 3%-Ba sample, where no Ti vacancies had been previously introduced in the system. Finally, V_0 remains nearly constant, meaning that no more europium is being incorporated inside the structure.

Thereby, from XRD results, we can conclude that the solubility limit of Eu^{3+} in compositions of both *Ba* and *Ti-mechanisms* is ≈ 3 mol% (which is in agreement with the previously cited investigations[3,9]) and that europium has the preference for occupying Ba^{2+} site. Above 3 mol%, the excess of dopant must be segregated as a secondary phase, but the small fraction of it may prevent an accurate identification using XRD[4] (except for 10%-Ti sample, where no single phase is obtained). Moreover, it is remarkable that, unlike micrometric materials prepared in other studies by the conventional ceramic route, the secondary phase $Eu_2Ti_2O_7$ has not been detected by XRD. For samples with a high content of Eu^{3+}, SEM/EDX analysis of the powders revealed the presence of some rod-like particles which were europium rich and could be attributed to secondary phases not detected by XRD.

3.2. Luminescence studies at room temperature

Structural characterisation results did not report significant changes for samples with Eu^{3+} concentrations above 3 mol%. Therefore, the optical characterisation at room temperature was carried out only for samples with Eu^{3+} content ≤ 4 mol%.

Room temperature emission spectra of the fired samples are depicted in Figure 3, where the emission bands are assigned to their respective transitions: $^5D_0 \rightarrow {}^7F_0$ (580 nm), $^5D_0 \rightarrow {}^7F_1$ (596 nm), $^5D_0 \rightarrow {}^7F_2$ (616 nm), $^5D_0 \rightarrow {}^7F_3$ (645–660 nm) and $^5D_0 \rightarrow {}^7F_4$ (680–715 nm), Figure 3(a). Spectra were collected upon excitation at the hypersensitive $^7F_0 \rightarrow {}^5D_2$ transition (466 nm) and were normalised to the magnetic dipole $^5D_0 \rightarrow {}^7F_1$ transition, whose intensity is often considered to be constant [15].

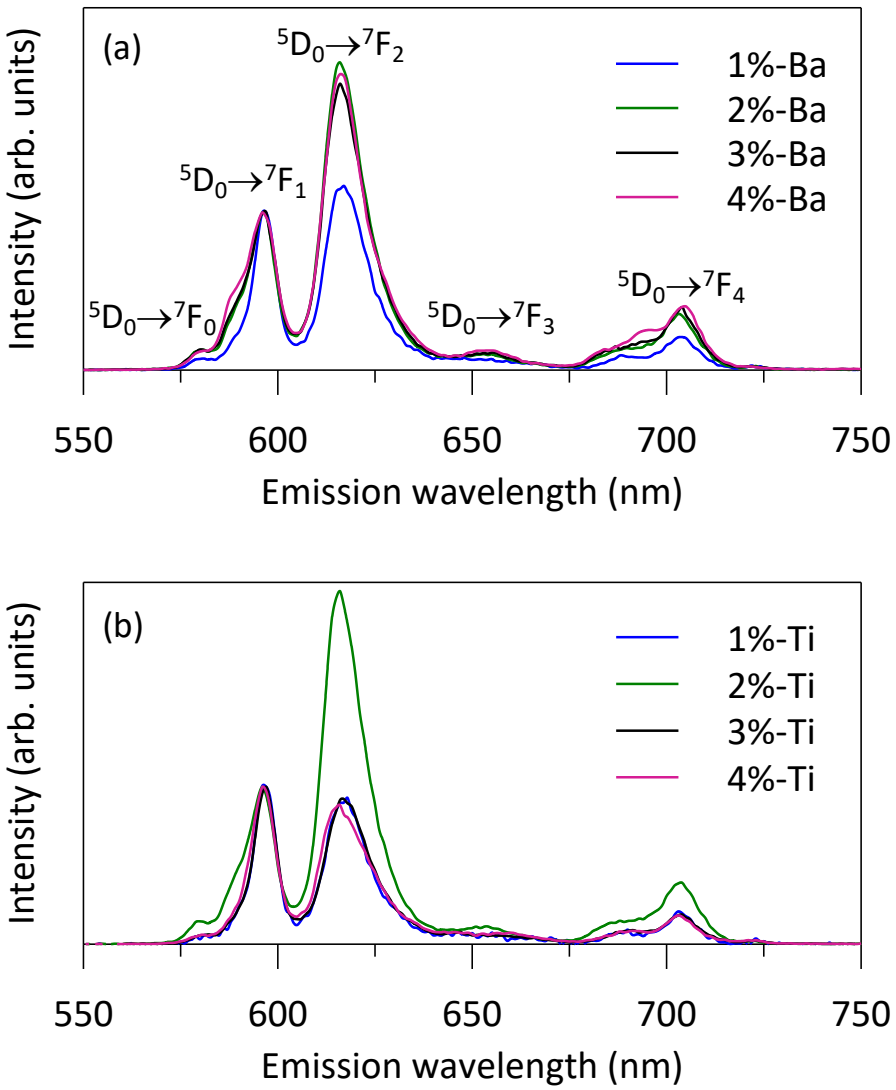

Figure 3. Room temperature emission spectra corresponding to the $^5D_0 \rightarrow {}^7F_{0\text{-}4}$ transitions of *Ba-mechanism* (a) and *Ti-mechanism* (b) samples obtained upon excitation at 466 nm.

As pointed out by literature [16,17], the Ω_2 Judd-Ofelt parameter is correlated to the polarizable and covalent character of the lanthanide ion in the lattice. Thus, the study of this parameter could contribute to shed some light on Eu^{3+} surroundings in the host

lattice. According to the Judd-Ofelt theory, the emission rate of a transition $i \rightarrow j$ can be expressed as

$$A_{ij} = \frac{64e^2\pi^4}{3h{\lambda_{ij}}^3} \cdot \frac{\chi}{(2J+1)} \cdot \sum_{\lambda=2,4,6} \Omega_\lambda \left\| U^\lambda \right\| \quad (1)$$

where λ_{ij} is the average wavelength of the transition $i \rightarrow j$; Ω_λ is the Judd-Ofelt parameter; $\left\| U^\lambda \right\|$ is an abbreviation of $\left| \langle \left\| U^\lambda \right\| \rangle \right|^2$, which corresponds to the reduced matrix elements of the unit tensor operator connecting states *i* and *j*; χ is the Lorentz local field correction term (which is equal to $\frac{n(n^2+2)^2}{9}$, *n* is the refractive index at λ_{ij}); *e* is the elementary charge; *h* is the Planck constant; and *J* refers to the state *i* [18].

On the basis of the experimental emission spectra, A_{0J} can be calculated using the expression

$$A_{0J} = A_{01} \cdot \frac{I_{0J}}{I_{01}} \cdot \frac{\lambda_{0J}}{\lambda_{01}} \quad (2)$$

where A_{01} is the magnetic dipole transition rate assumed constant and equal to 50 s^{-1}; *I* and λ are the intensity and the wavelength value of the transition $0 \rightarrow J$, respectively.

A combination of expressions (1) and (2) for the $^5D_0 \rightarrow {}^7F_2$ transition results in

$$\Omega_2 = A_{01} \cdot \frac{I_{02}}{I_{01}} \cdot \frac{{\lambda_{02}}^4}{\lambda_{01}} \cdot \frac{3h}{64e^2\pi^4 \, \chi \left\| U^2 \right\|} \quad (3)$$

The ratio *R* is defined as the ratio between the intensities of $^5D_0 \rightarrow {}^7F_2$ and $^5D_0 \rightarrow {}^7F_1$ transitions:

$$R = \frac{I_{02}}{I_{01}} \quad (4)$$

Thereby, we can rewrite expression (3) as follows

$$\Omega_2 = A_{01} \cdot R \cdot \frac{{\lambda_{02}}^4}{\lambda_{01}} \cdot \frac{3h}{64e^2\pi^4 \, \chi \left\| U^2 \right\|} \quad (5)$$

The value reported in the literature for $\left\| U^2 \right\|$ is 0.0032 [19]. The average wavelength value obtained for samples is 596 nm for λ_{01} ($^5D_0 \rightarrow {}^7F_1$ transition) and 616 nm for λ_{02} ($^5D_0 \rightarrow {}^7F_2$ transition). The refractive index of $BaTiO_3$ at 616 nm is 2.4122 [20]. Expressing λ_{0J} in cm, taking *h* = $6.6261 \cdot 10^{-27}$ erg·s, *e* = $4.803 \cdot 10^{-10}$ esu [21] and substituting the rest of values, Ω_2 can be expressed as

$$\Omega_2 = (3.1844\, R) \cdot 10^{-21}\ \text{cm}^2 \quad (6)$$

Higher values of Ω_2 suggest that the environment around europium in $BaTiO_3$ structure is more polarizable and covalent [16]. The ionic radius and CN for Ba^{2+} are higher than for Ti^{4+}. In this way, there will be more electronic distortion around Eu^{3+} in Ba^{2+} site, which means that the ion will be more polarizable. Therefore, higher values of Ω_2 are expected if a great majority of Eu^{3+} ion occupies Ba^{2+} site. *R* and Ω_2 values are summarised in Table 2 for samples of both mechanisms and Ω_2 evolution with Eu^{3+} concentration is plotted in Figure 4.

Table 2. *R* and Ω_2 values obtained from emission spectra at room temperature (λ_{exc} = 466 nm).

Sample	*R*	Ω_2 (10^{-21} cm^2)	Sample	*R*	Ω_2 (10^{-21} cm^2)
1%-Ba	1.17	3.7	1%-Ti	0.93	3.0
2%-Ba	1.95	6.2	2%-Ti	2.24	7.1
3%-Ba	1.82	5.8	3%-Ti	0.92	2.9
4%-Ba	1.88	6.0	4%-Ti	0.88	2.8

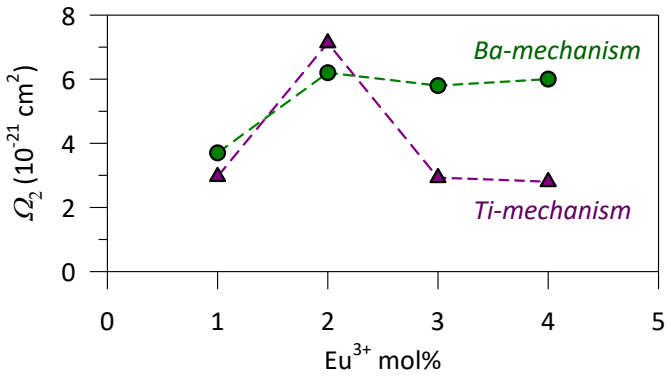

Figure 4. Ω_2 evolution with Eu^{3+} concentration for samples of *Ba* and *Ti-mechanism*.

From the analysis of Ω_2 evolution with Eu^{3+} content, similar conclusions as the ones obtained by XRD can be drawn. For *Ba-mechanism* samples, there is an increase in Ω_2 until a concentration of 2 mol% Eu^{3+} is reached. Then, the Judd-Ofelt parameter remains nearly constant, implying there are no noticeable changes in the polarizability environment of the ion, an aspect closely related with the solubility limit. In addition, it is particularly noteworthy that *Ti-mechanism* samples follow the same tendency up to 2

mol% Eu^{3+} as well. Therefore, the crystal field of Eu^{3+} must be quite similar, suggesting that europium occupies the same sites of substitution in this range of concentrations. Linking these results with XRD analysis, we can conclude that the preference of Eu^{3+} is to occupy Ba^{2+} site up to 2% regardless of the nominal composition of the mechanism postulated.

For *Ti-mechanism* samples, a sharp decline in Ω_2 is produced at 3 mol% of Eu^{3+}, which indicates the dopant has suffered a reorganisation inside the structure due to the crystal field acting on it is different. Given that above 3 mol% of dopant, the Judd-Ofelt parameter is almost constant, it is confirmed that the solubility limit of Eu^{3+} in $BaTiO_3$ for the proposed mechanisms is about 3 mol%.

3.3. FLN spectra

3.3.1. Experimental results

In spite of the room temperature spectroscopic results shown in section 3.2 by using a conventional spectrometer, low temperature site-selective excitation of Eu^{3+} performed by using time-resolved fluorescence line-narrowing (TRFLN) technique in cation-defective $BaTiO_3$ samples, displays a very complex behaviour which points to the existence of at least five different defined crystal field sites for the lanthanide ion. In order to simplify the description of the different sites and following the standard acronym ABX_3 to describe perovskite oxides, we shall call A_i and B_i the lanthanide substitutional centres in $BaTiO_3$ matrix when Eu^{3+} occupies the Ba^{2+} and Ti^{4+} sites, respectively.

As an example, Figure 5 shows a selection of the low temperature (10 K) TRFLN spectra corresponding to the $^5D_0 \rightarrow {}^7F_{0\text{-}2}$ transitions of 1%-Ba sample obtained with a time delay of 10 μs after the pump pulse (~0.08 cm^{-1} spectral width) at three different pumping wavelengths along the $^7F_0 \rightarrow {}^5D_0$ transition. As can be seen, depending on the excitation wavelength the emission spectra present different characteristics, regarding the number of observed $^5D_0 \rightarrow {}^7F_J$ components, their relative intensity, and the magnitude of the observed crystal-field splitting for each ^7F_J state. Starting from the bottom, the 1%-Ba(Site A_1) spectrum obtained by pumping at 579.05 nm displays, besides the single component of the resonant $^5D_0 \rightarrow {}^7F_0$ emission, a three-component emission corresponding to the $^5D_0 \rightarrow {}^7F_1$ magnetic dipole transition and a weaker emission from the $^5D_0 \rightarrow {}^7F_2$ electric

dipole emission. It is worthy to notice the strong intensity of the $^5D_0 \rightarrow {}^7F_0$ emission suggesting the presence of large linear terms in the crystal field potential. The 1%-Ba(Site A_2) spectrum measured by pumping at 579.20 nm exhibits a single $^5D_0 \rightarrow {}^7F_1$ emission peak with the highest intensity among all the observed $^5D_0 \rightarrow {}^7F_J$ transitions with a weak contribution from the electric dipole $^5D_0 \rightarrow {}^7F_2$ emission. Finally, the 1%-Ba(Site A_3) spectrum obtained by exciting at 579.35 nm shows a prominent $^5D_0 \rightarrow {}^7F_0$ resonant emission together with a two-component $^5D_0 \rightarrow {}^7F_1$ emission accompanied by a weak $^5D_0 \rightarrow {}^7F_2$ contribution.

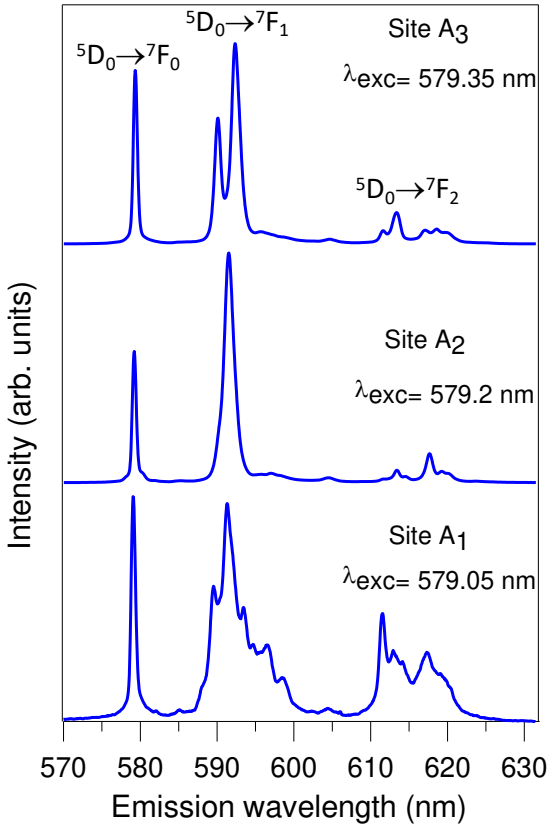

Figure 5. Low temperature (10 K) TRFLN spectra corresponding to the $^5D_0 \rightarrow {}^7F_{0\text{-}2}$ transitions of 1%-Ba sample obtained with a time delay of 10 μs after the pump pulse at three different pumping wavelengths.

The 2%-Ba and 2%-Ti samples show similar emission sites with the proviso that A_1 site is more sharply defined. It is worthwhile noticing that the increase of Eu^{3+}doping in the 2%-Ba sample increases the emission efficiency of site A_1, whereas A_2 and A_3 sites are not much affected. In the case of the 1%-Ti and 2%-Ti sample (not shown in the Figure), no

significant differences can be observed for the three A_1, A_2 and A_3 sites (pumping wavelengths and emission intensities) if compared with those found in the 1%-Ba sample.

The spectral behaviour of 3%-Ba and 3%-Ti samples, displayed in Figure 6(b), deserves special comments because here, in agreement with the previous X-ray diffraction and spectroscopic results of sections 3.1 and 3.2, significant changes in the crystal field around the lanthanide ions seem to take place. In particular, site A_1 disappears in the 3%-Ti sample whereas a new one of similar characteristics (Site B_1) appears at longer wavelengths and another one (Site B_2, red stars in Figure 6) clearly emerges at the long wavelength tail of the $^5D_0 \rightarrow {}^7F_1$ emission of the main site A_2. This new site, which also weakly appears (less pronounced) in the 3%-Ba sample, has the longest lifetime of all the observed emissions as we shall next see.

In conclusion, in the 3%-Ba and 3%-Ti samples, we have found three different *A*-type and two different *B*-type crystal field sites for Eu^{3+} ion, whose nature is discussed below and summarised in Table 3.

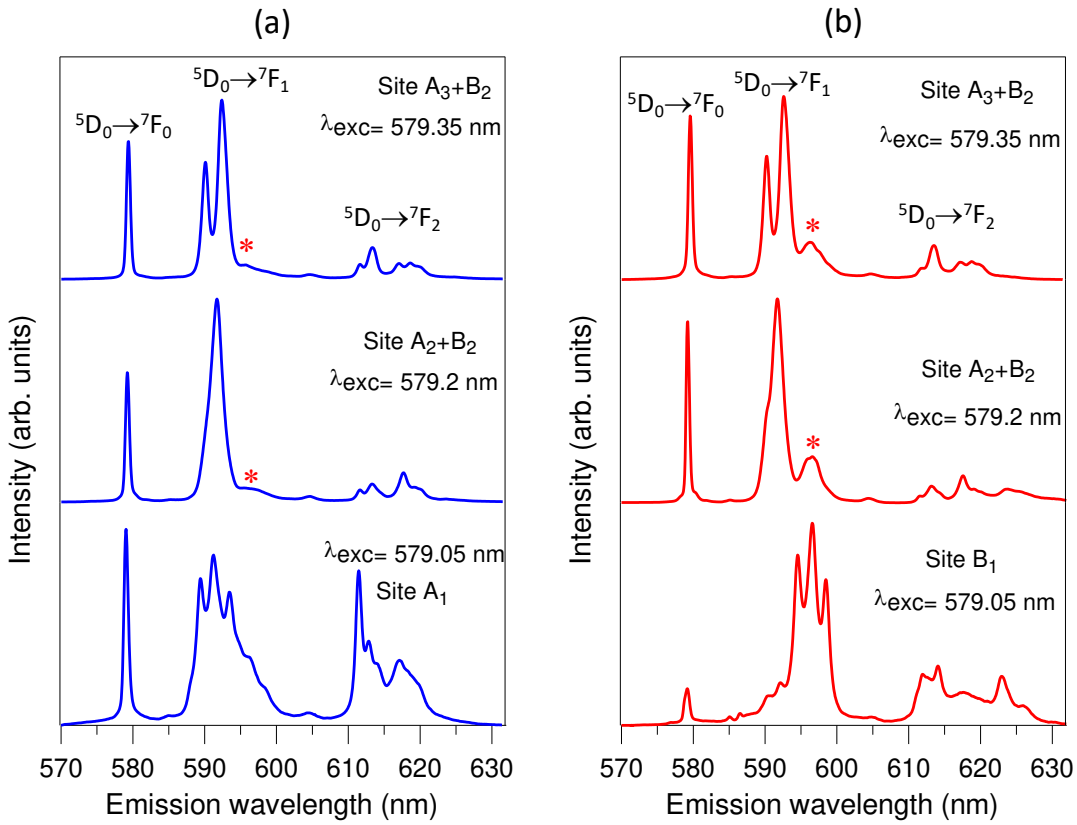

Figure 6. $^5D_0 \rightarrow {}^7F_{0\text{-}2}$ emission spectra of samples 3%-Ba (a) and 3%-Ti (b) showing the emissions from sites A_1, A_2, A_3, B_1, and B_2 (red stars).

Table 3. Description of the different crystal field sites for Eu^{3+} ion in doped-$BaTiO_3$ samples. The abbreviations A_i and B_i refer to Eu^{3+} occupying Ba^{2+} and Ti^{4+} sites, respectively.

λ_{exc} (nm)	Sites	Symmetry
579.05	A_1	Low (nearby particle surface)
	B_1	Low (nearby particle surface)
579.20	A_2	Close to cubic
	B_2	Cubic (O_h)
579.35 [a]	A_3	Trigonal (C_{3v} or C_3)

[a] The emission of Site B_2 can also be observed when pumping at 579.35 nm due to vibronic coupling.

3.3.2. On the origin and symmetries of the Eu^{3+}sites in barium titanate

The spectroscopic response of Ln^{3+} impurity centers in a solid-state material depends on the local atomic environment. Additionally, in the case of micro-nanostructures, where the surface to volume ratio changes as a function of the particle size, lattice deformations near the surface may produce variable Ln^{3+} environments even if Ln^{3+} ions occupy substitutional sites and, as a consequence, different crystal field sites and/or glassy-like disorder can be observed in the Ln^{3+} emission spectrum. In the case of Eu^{3+}doped $BaTiO_3$ powders, the main luminescence emission is usually attributed to the Ln^{3+} occupying a Ba^{2+} substitutional site, though, as we have discussed above, *B* site occupancy is also expected for Ln^{3+} ions [4,8,22,23]. At low temperature (10 K) in the rhombohedral phase, account taken of the smaller ionic radius of Eu^{3+}, if compared to the one of barium, we expected the appearance of defects to compensate the excess of charge introduced by the Ln^{3+} ion. Therefore, we could guess a symmetry lowering at the substitutional site from the cubic symmetry class at high temperature [24]. However, EPR studies performed in Gd^{3+}-doped $BaTiO_3$ (both $Eu^{3+}$and Gd^{3+} have similar ionic radius), confirm that the lanthanide substitutes the alkali earth ion with no remarkable distortion effects [25]. In the particular case of europium-doped barium titanate prepared by the sol-gel method, only a few works discuss the presence of some glassy-like spectral disorder when exciting at a direct Ln^{3+} level [26,27], and only a few of them deal with the problem of the amphoteric behavior of Eu^{3+} ion [4,8,22].

As can be seen in Figures 5 and 6, the low-temperature structure of the time-resolved emission spectra shows the existence of low symmetry sites: A_1 present in all (1,2,3)-%Ba and (1,2)-%Ti samples, and B_1 in the 3%-Ti sample. Site A_1 would be related to Eu^{3+} ions occupying a substitutional Ba^{2+} site in a highly distorted environment in a thin shell nearby the surface of the nano-micro particle, whereas B_1, with a similar $^5D_0 \rightarrow {}^7F_1$ emission, but appearing at longer wavelengths, could be associated to lanthanide occupancy of a distorted Ti^{4+}crystal field site [23]. The existence of distorted crystal field sites nearby the particle surface have also been observed in Eu^{3+}-doped oxide powders [28]. On the other hand, site A_2 shows the most intense and single component $^5D_0 \rightarrow {}^7F_1$ emission, with a very small contribution from the electric dipole $^5D_0 \rightarrow {}^7F_2$ transition, which would suggest the presence of a high symmetry anion distribution around the lanthanide. In fact, the high coordination number of the Ba^{2+} ion (CN=12) tends to increase the effective site symmetry and as a consequence reduces and/or suppresses the crystal field splitting. However, the presence of a strong $^5D_0 \rightarrow {}^7F_0$ peak and several intense $^5D_0 \rightarrow {}^7F_4$ emission components excludes formally cubic point symmetry groups at site A_2. However, it is worth noticing that, as pointed in reference [24], in the low-temperature rhombohedral phase, the $BaTiO_3$ unit cell form is close to the high-temperature cubic one. In conclusion, at least, at low temperature, the point symmetry of site A_2 is close to a cubic one.

Referring to site A_3, in both 3%-Ba and 3%-Ti samples, the FLN spectra in Figure 6 show a two components emission for the $^5D_0 \rightarrow {}^7F_1$ transition and five $^5D_0 \rightarrow {}^7F_4$ components (not shown in the Figure), being this result therefore compatible with a C_{3v} point group symmetry. We notice that the bump appearing at the long wavelength tail of the $^5D_0 \rightarrow {}^7F_1$ emission in both A_2 and A_3 sites (marked with a red star), which is enhanced in the 3%-Ti sample, corresponds to site B_2 discussed below.

Figure 7 displays the time-resolved spectra corresponding to the $^5D_0 \rightarrow {}^7F_{0\text{-}2}$ emissions of both 3%-Ba and 3%-Ti samples by exciting at 579.20 nm, the wavelength used for exciting site A_2. As can be observed, as time evolves, the main features of site A_2 tend to disappear whereas the bump at the low energy side of the $^5D_0 \rightarrow {}^7F_1$ emission peak grows and becomes the only remaining spectral component at 596.9 nm. It is worth noticing that the lifetime of this component is longer than 12 ms, the temporal range of our optical multichannel analyser. This weak emission would thus correspond to the new

Eu^{3+} crystal field site, B_2, mentioned before. The absence of other spectral components, including the $^5D_0 \rightarrow {}^7F_0$ emission, points to a cubic point symmetry group for this site. It is important to mention that, as Figure 6 shows, this emission can also be observed when pumping site A_3 at 579.35 nm. This would suggest the presence of a strong enough vibronic coupling that would allow the cubic site to be pumped through the vibronic sidebands of the electronic level. In good agreement with these facts, our FLN measurements confirm the presence of anti-Stokes and Stokes vibronic sidebands in the $^5D_0 \rightarrow {}^7F_0$ (peaking at around 38 and 63 cm^{-1} from the $^5D_0 \rightarrow {}^7F_0$ main peak at 17265 cm^{-1}) and $^5D_0 \rightarrow {}^7F_1$ (anti-Stokes at 119 and Stokes at 146 cm^{-1} vibronic sidebands) transitions. As an example, Figure 8 shows the emission of site A_2 by pumping its anti-Stokes vibronic band at 577.9 nm in the 1%-Ba sample. These broad vibronic bands, together with the inherent disorder introduced by charge compensation, promote the observed glassy-like disorder when not pumping at the precise wavelength of the electronic transition.

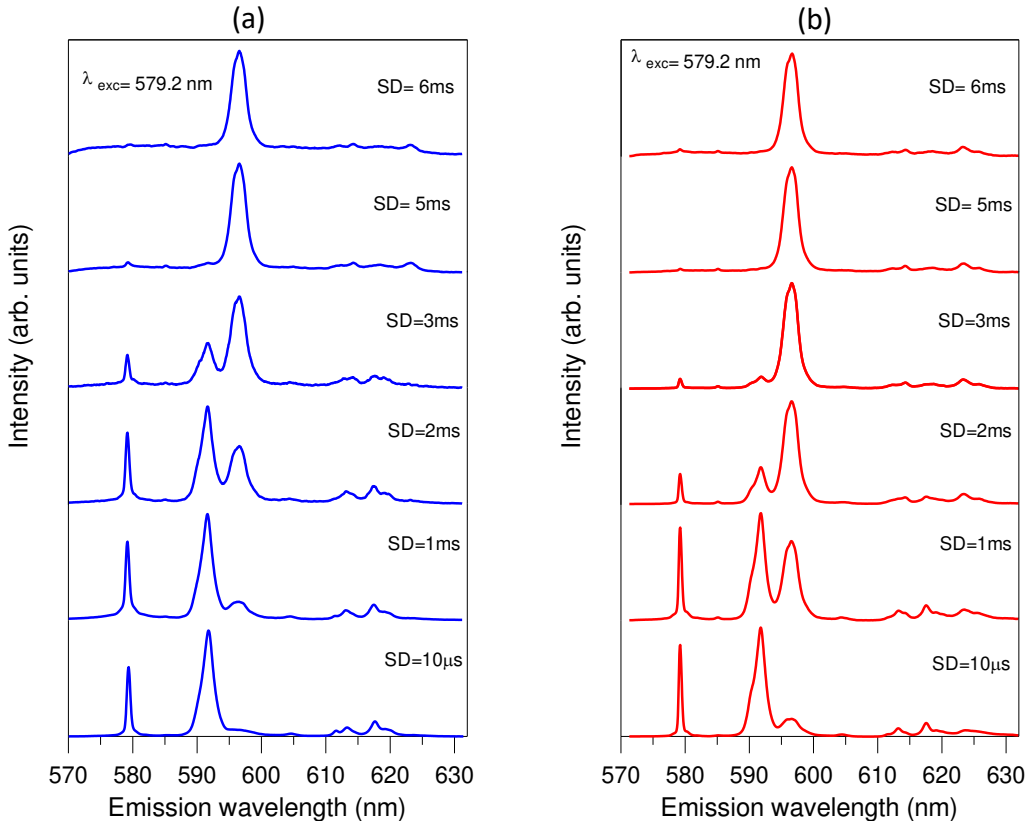

Figure 7. Time-resolved $^5D_0 \rightarrow {}^7F_{0\text{-}2}$ emission spectra of A_2+B_2 sites in both 3%-Ba (a) and 3%-Ti (b) samples excited at 579.2 nm.

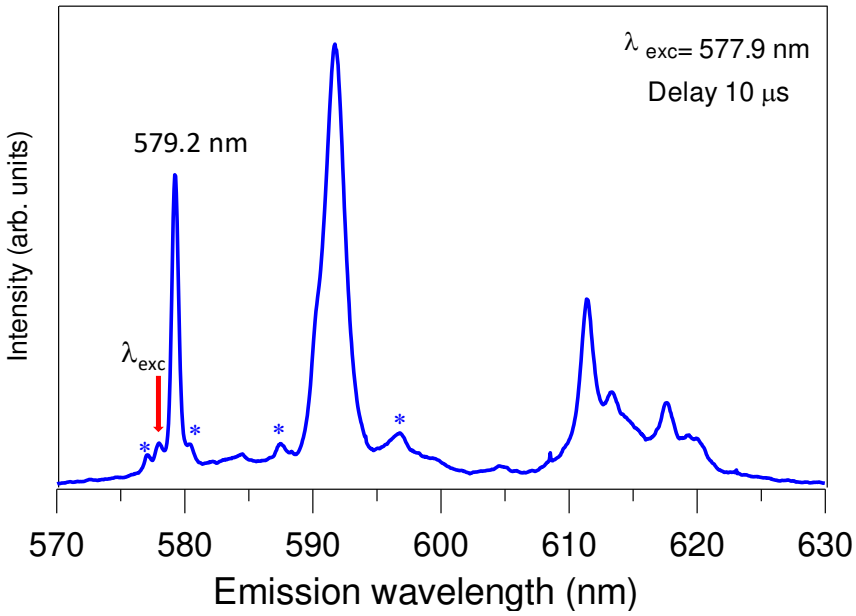

Figure 8. $^5D_0 \rightarrow {}^7F_{0\text{-}2}$ emission spectrum of site A_2 by pumping its anti-Stokes vibronic band at 577.9 nm in the 1%-Ba sample. The stars point out the vibronic components of the $^5D_0 \rightarrow {}^7F_{0\text{-}1}$ transitions.

Referring to the expected charge compensation mechanisms associated with Ln^{3+} doping, different possibilities have been proposed. In our case, oxygen vacancies are not expected to play a significant role, as samples were sintered in an air atmosphere. Thus, as we shall next see, the plausible mechanisms could be close to those proposed in references [4,8,22]. These authors, based on theoretical and experimental measurements, have suggested the existence of europium sites *A* assuming Ti^{4+} vacancies or a self-compensation mechanism produced by Eu^{3+} pairs substituting Ba and Ti crystal sites (mechanisms 2 and 3 of Figure 1).

We shall first focus on the main A_2 site, disregarding the low crystal field symmetry of A_1 and B_1 sites due to the lattice deformation nearby the particle surface. In spite of the smaller ionic radius of Eu^{3+} (r_{Eu}= 1.226 Å with CN=12) if compared with the one of Ba^{2+} (r_{Ba}= 1.610 Å), the apparent high symmetry of this site is only compatible with a very low distorted oxygen coordination, meaning that the unit cell centered at the Ln^{3+} ion could be neither titanium defective nor self-compensated by a Ln_{Ba}+Ln_{Ti} pair [8,22].

This result suggests that the compensation mechanism would be located in cells neighboring the defect carrier. But in the case the unit cell would present a Ti^{4+}vacancy and/or a substitutional Eu^{3+} pair, it would be still possible to keep a trigonal axis of

symmetry along the Ln-Ln or Ln-Ti (vacancy) diagonal of the unit cell which would lower the symmetry to C_{3v} or C_3, giving rise to the observed symmetry of site A_3.

Referring to site B_2, its features are only compatible with a high symmetry octahedral crystal field site associated with the Ti^{4+}substitution by Eu^{3+}. As the octahedral coordinated ionic radius of Eu^{3+} (0.947 Å) is higher than the one of Ti^{4+} (0.605 Å), we expect a stronger cation-anion interaction giving rise to a highly symmetric crystal field around the Eu^{3+} ion. Moreover, the stronger Eu-O interaction at the Ti^{4+} site, if compared with the one at site Ba^{2+}, makes potential energy curves of Eu^{3+} centers to become steeper at the Ti^{4+} sites if compared to those of Eu^{3+}at Ba^{2+}sites, giving rise to the observed red-shift of the Eu^{3+}emission bands at the Ti^{4+} sites. Finally, the notable increase of the unit cell volume in the 3%-Ti sample associated with the Ln^{3+} substitution would explain the limited amount allowed for Eu^{3+} substitutions at B_2 sites.

4. Conclusions

The crystallographic nature and spectroscopic properties of non-equivalent europium sites in $BaTiO_3$ have been investigated. Samples were synthesised via sol-gel in accordance with the nominal formula of two possible substitution mechanisms: $(Ba_{1-3x}Eu_{2x})TiO_3$ and $Ba(Ti_{1-x}Eu_x)O_{3-x/2}$. Bearing in mind the adequacy of the dopant ion as a structural probe, site-selective excitation within the inhomogeneous broadened $^7F_0 \rightarrow {}^5D_0$ absorption band was performed. The obtained results allow us to draw the following conclusions:

- The solubility limit of Eu^{3+} in $BaTiO_3$ samples has been found to be 3 mol%.

- The preference of Eu^{3+} is to occupy Ba^{2+} sites regardless of the nominal compositions and substitution mechanism. The main luminescence emission can be attributed to Eu^{3+} occupying Ba^{2+} substitutional sites; in particular, site A_2 is the most efficient emitter. Besides, Ti^{4+} sites occupancy has also been proved by their FLN emission.

- XRD data and Ω_2 Judd-Ofelt parameters are in agreement with the site-selective excitation results. In all experiments, a clear difference appears between 3%-Ba and 3%-Ti samples. The V_0 increase and the Ω_2 decline in the 3%-Ti sample is consistent

with a greater proportion of Eu^{3+} ions occupying Ti^{4+} sites. This result would explain the limited amount allowed for Eu^{3+} substitutions at B_2 sites.

- TRFLN spectra show the presence of five different europium crystal field sites and possible crystal symmetries have been inferred for each one.

- TRFLN measurements confirm the presence of relatively strong anti-Stokes and Stokes vibronic sidebands in the $^5D_0 \rightarrow {}^7F_{0,1}$ transitions. This important issue can explain the lack of site resolution found in the room temperature spectra of these transitions, obtained by selective pumping of the hypersensitive $^5D_2$ level, due to the vibronic mixing of the excited levels.

All things considered, this study highlights the amphoteric behaviour of Eu^{3+} in $BaTiO_3$. As it has been reported in literature [3], noticeable changes for both electric and magnetic properties of the material are observed depending on the site occupancy of dopants. Thereby, the presence of different crystallographic sites for Eu^{3+} could have a decisive impact not only on the optical properties of $BaTiO_3$ ceramics but also on their wide range of electronic properties and device applications.

Acknowledgements

P.S-G, H.B-M and E.C. thank the Universidad Jaume I (Project UJI-B2016-38) and Ministerio de Economía y Empresa (Project MAT2016-80410-P) for financial support. P.S-G also thanks Universidad Jaume I for a fellowship. R.B. and J. F. acknowledge financial support from MINECO under Project MAT2017-87035-C2-2-P (AEI/FEDER, UE), Basque Country University PPG17/07 and GIU17/014, and Basque Country Government PIBA2018-24.

References

1 D. Sitko, *Phase Transitions*, 2014, **87**, 1002–1010.

2 J. Reyes Miranda, A. García Murillo, F. de J. Carrillo Romo, J. Oliva Uc, C. A. Flores

Sandoval, A. de J. Morales Ramírez, S. Velumani, E. de la Rosa Cruz and V. Garibay Febles, *J. Sol-Gel Sci. Technol.*, 2014, **72**, 435–442.

3 A. Ahad, M. A. Taher, M. K. Das, M. Z. Rahaman and M. N. I. Khan, *Results Phys.*, 2019, **12**, 1925–1932.

4 F. A. Rabuffetti, S. P. Culver, J. S. Lee and R. L. Brutchey, *Nanoscale*, 2014, **6**, 2909–2914.

5 T. D. Dunbar, W. L. Warren, B. A. Tuttle, C. A. Randall and Y. Tsur, *J. Phys. Chem. B*, 2004, **108**, 908–917.

6 L. A. Xue, Y. Chen and R. J. Brook, *Mater. Sci. Eng. B*, 1988, **1**, 193–201.

7 M. T. Buscaglia, V. Buscaglia, P. Ghigna, M. Viviani, G. Spinolo, A. Testino and P. Nanni, *Phys. Chem. Chem. Phys.*, 2004, **6**, 3710–3713.

8 D. Y. Lu, T. Ogata, H. Unuma, X. C. Li, N. N. Li and X. Y. Sun, *Solid State Ionics*, 2011, **201**, 6–10.

9 M. K. Rath, G. K. Pradhan, B. Pandey, H. C. Verma, B. K. Roul and S. Anand, *Mater. Lett.*, 2008, **62**, 2136–2139.

10 D.-Y. Lu, T. Koda, H. Suzuki and M. Toda, *J. Ceram. Soc. Japan*, 2005, **113**, 721–727.

11 C. Cascales, R. Balda, V. Jubera, J. P. Chaminade and J. Fernández, *Opt. Express*, 2008, **16**, 2653–2662.

12 C. Cascales, P. Porcher, J. Fernandez, A. Oleaga, R. Balda and E. Dieguez, *J. Alloys Compd.*, 2001, **324**, 260–266.

13 C. Cascales, J. Fernández and R. Balda, *Opt. Express*, 2005, **13**, 2141.

14 A. R. W. Héctor Beltrán, Eloisa Cordoncillo, Purificación Escribano, Derek C. Sinclair, *J. Am. Ceram. Soc*, 2004, **87**, 2132–2134.

15 K. Binnemans, *Coord. Chem. Rev.*, 2015, **295**, 1–45.

16 D. K. Patel, B. Vishwanadh, V. Sudarsan and S. K. Kulshreshtha, *J. Am. Ceram. Soc.*, 2013, **96**, 3857–3861.

17 C. de Mello Donega, S. A. Junior and G. F. de Sa, *J. Alloys Compd.*, 1997, **250**, 422–426.

18 B. Julián, J. Planelles, E. Cordoncillo, P. Escribano, P. Aschehoug, C. Sanchez, B. Viana and F. Pellé, *J. Mater. Chem.*, 2006, **16**, 4612–4618.

19 *Ann. West Univ. Timisoara - Phys.* , 2012, 56, 127.

20 Mikhail N. Polyanskiy, Refractive index database.

21 Y. H. Elbashar and D. A. Rayan, *Int. J. Appl. Chem.*, 2016, **12**, 59–66.

22 C. L. Freeman, J. A. Dawson, H. R. Chen, J. H. Harding, L. Bin Ben and D. C. Sinclair, *J. Mater. Chem.*, 2011, **21**, 4861–4868.

23 S. Makishima, K. Hasegawa and S. Shionoya, *J. Phys. Chem. Solids*, 1962, **23**, 749–757.

24 H. Yamamoto, S. Makishima and S. Shionoya, *J. Phys. Soc. Jpn*, 1967, **23**, 1321–1332.

25 L. Rimai and G. A. DeMars, *Phys. Rev.*, 1962, **127**, 702–710.

26 W. Strek, D. Hreniak, G. Boulon, Y. Guyot and R. Pązik, *Opt. Mater. (Amst).*, 2003, **24**, 15–22.

27 D. Hreniak, W. Strek, J. Amami, Y. Guyot, G. Boulon, C. Goutaudier and R. Pazik, *J. Alloys Compd.*, 2004, **380**, 348–351.

28 C. Cascales, R. Balda, S. García-Revilla, L. Lezama, M. Barredo-Zuriarrain and J. Fernández, *Opt. Express*, 2018, **26**, 16155.